Intrinsic photomixing detector based on amorphous silicon for envelope mixing of optical signals

Cite as: APL Photon. 8, 086101 (2023); doi: 10.1063/5.0149024
Submitted: 3 March 2023 • Accepted: 10 July 2023 •
Published Online: 1 August 2023

Maurice Müller,[1,a] Andreas Bablich,[2,b] Rainer Bornemann,[1,c] Nils Marrenbach,[1,d] Paul Kienitz,[2,e] and Peter Haring Bolívar[1,f]

AFFILIATIONS

[1] Institute of High Frequency and Quantum Electronics, Faculty IV: School of Science and Technology, University of Siegen, Hölderlinstr. 3, 57076 Siegen, Germany
[2] Institute of Graphene-Based Nanotechnology, Faculty IV: School of Science and Technology, University of Siegen, Hölderlinstr. 3, 57076 Siegen, Germany

[a] **Author to whom correspondence should be addressed:** Maurice.mueller@uni-siegen.de
[b] andreas.bablich@uni-siegen.de
[c] rainer.bornemann@zess.uni-siegen.de
[d] nils.marrenbach@student.uni-siegen.de
[e] paul.kienitz@uni-siegen.de
[f] peter.haring@uni-siegen.de

ABSTRACT

In this work, a promising device for direct optical envelope mixing, the Intrinsic Photomixing Detector (IPD) based on hydrogenated amorphous silicon, is reported. The IPD directly generates a photocurrent proportional to the nonlinear mixing of two optical modulation envelope functions. Experiments illustrate efficient mixing in the visible range at low light levels down to $\phi_1 = 4.36\ \mathrm{mW/cm^2}$ (444 nm) and $\phi_2 = 1.03\ \mathrm{mW/cm^2}$ (636 nm). Modulation frequencies exceeding the MHz range are demonstrated. Electro-optical simulations identify defect-induced electrical field screening within the absorber to cause the nonlinear mixing process, opening-up the opportunity to tailor devices toward application-specific requirements. The IPD functionality paves the way toward very simple but high-performance photodetectors for 3D imaging and ranging for direct optical convolutional sensors or for efficient optical logic gates. Using amorphous silicon provides a photodetector material base, which can easily be integrated on top of silicon electronics, enabling fill factors of up to 100%.

INTRODUCTION

Within the last few decades, hydrogenated amorphous silicon (a-Si:H) attracted wide research interest in fields of optoelectronic applications, e.g., solar cells,[1] thin-film transistors,[2] photodetection,[3] or multispectral sensing,[4] due to its high absorption coefficient in the visible range,[5] versatile bandgap tuning,[6,7] low-temperature manufacturing,[8] and doping[9] capabilities. Besides classical application examples, a-Si:H has recently gained interest in the field of optical communication systems as this class of material enables wavelength conversion at high data rates due to nonlinear optical processes.[10] In a-Si-H waveguides, optical (N)AND logic gate operation in the time domain at GHz frequencies has already been demonstrated utilizing four-wave mixing Bragg scattering, a third-order nonlinear process.[11] Mixing processes, such as heterodyning, are also applicable in the RF[12,13] and RADAR technology.[14] Furthermore, frequency mixing techniques are well-established, e.g., to generate THz radiation.[15] However, this principle requires expensive, high intense laser sources and a nonlinear medium[10,16,17] or device[18] to mix the frequencies of the stimulating radiation. High-speed nonlinear graphene-based devices have been reported for mixing the envelope of two optical signals[19] or an electrical signal and an optical modulated signal[20,21] achieving modulation bandwidth in the GHz range. Besides lacking scalability and reproducibility, the 2D-material-based approach actually suffers from low efficiencies so that typically irradiances exceeding 100 $\mathrm{mW/cm^2}$ are required.[20]

Furthermore, established envelope frequency mixing devices, such as the photonic mixer device used for 3D imaging, utilize a smart but rather complex device architecture and signal processing to realize sum/differential frequency generation of an optical signal and an additional electrical signal.[22] Although this technology is highly approved, it has drawbacks due to the complexity so that geometrical fill factors stagnate at ~22% due to extensive electrical circuitry.[23]

In contrast to these techniques, we propose a very simple and scalable low-cost approach to mix the envelope intensity of two amplitude modulated light sources by utilizing a well-designed field optimized a-Si:H p–i–n photodiode, the Intrinsic Photomixing Detector (IPD) [cf. Fig. 1(a)]. For that, electro-optical simulation models have been developed to study and optimize the device structure and physics. The simulation results are presented in the section titled Electro-optical simulation. The proposed detector enables envelope intensity mixing at irradiances below 5 mW/cm^2 and modulation frequencies exceeding MHz. Besides 3D imaging and optical ranging capabilities, we identify potential key applications of this device in fields of optical communication systems and optical (analog) computing. Optical AND logic gate functionality derived from a frequency analysis is demonstrated in the supplementary material. The mature thin-film process technology further allows for low-temperature sensor integration on top of silicon electronics with pixel fill factors of 100%.[24,25]

ELECTRO-OPTICAL SIMULATION

Photogating

A comprehensive electro-optical simulation model of modulated dual-light-beam current measurements on the IPD based on a-Si:H has been developed using the software AFORS-HET.[26] Further details on the simulation model are given in Ref. 27 and in the section titled Methods. This model enables establishing a consecutive understanding of charge carrier generation and transport processes within the sensor structure at different illumination scenarios. Steady-state simulation results of the internal electric field profile $E(x)$ across the intrinsic layer (i-layer) for varying wavelengths and in the dark state are given in Fig. 1(b). The local electrical field particularly determines the overall charge collection efficiency since an absolute low (or even positive) internal *E-field* prevents charges to be transported toward the respective electrical contact. In the dark state, the electrical field profile coincides with Crandall's non-uniform field theory.[28] Depending on the illumination scenario, a photo-induced internal charge transport barrier is generated due to deep trap-induced screening of the built-in field in a-Si:H photodiodes.[27,29,30] That barrier is located at a position $x = x_{E=0}$ where the *E-field* vanishes or becomes positive. Electrons that are generated within the i-layer region surrounded by the p-doped layer and $x_{E=0}$ are not able to drift toward the n-type a-Si:H. In result, these electrons will not contribute to a photocurrent. To derive a physical understanding of the envelope mixing in the a-Si:H IPD, we propose and define a charge carrier collection zone with the length x_{cz} starting at the position $x_{E=0}$ and ending at the i–n interface (here: $x = x_i = 1520$ nm) at the rear end of the detector. If the illumination scenario does not result in a *E-field* collapse ($E < 0$ for $0 \leq x \leq x_i$), the collection zone x_{cz} and the i-layer thickness x_i become equal. Dichromatic or multispectral illumination can result in a huge collection zone expansion and hence to a significant increase in the photocurrent compared to monochromatic illumination, as shown in Fig. 1(b) and Refs. 31–33. For simulations, dichromatic illumination with wavelengths in the visible range of $\lambda_1 = 444$ nm ($\phi_1 = 14.8$ mW/cm^2) and $\lambda_2 = 636$ nm ($\phi_2 = 42.4$ mW/cm^2) have been used to demonstrate the field enhancement principle for this specific detector and absorber composition. The specific *E-field* characteristics result in a nonlinear photoresponse for that illumination scenario. In this case, the collection zone length and the intrinsic absorber thickness become equal $x_{cz} = x_i = 1526$ nm [cf. pink line, Fig. 1(b)], whereas a quenching and vanishing electric field at $x_{E=0}$ occurs for monochromatic 444 nm illumination, only. In the latter case, a field reversal at the position $x_{E=0}$ takes place reducing the collection

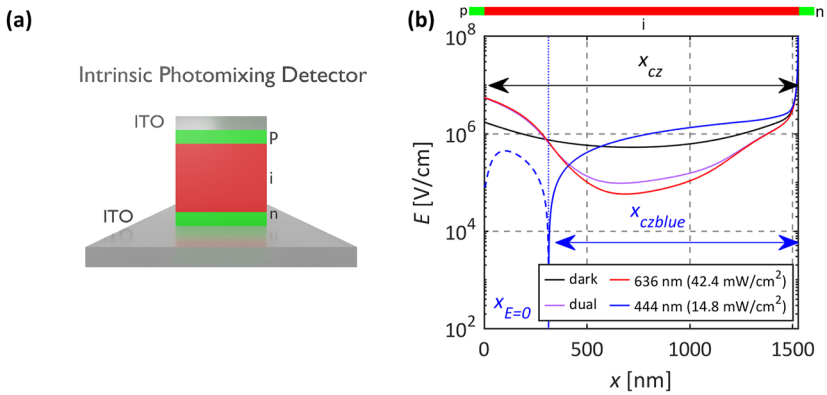

FIG. 1. (a) Schematic of the Intrinsic Photomixing Detector (IPD) consisting of an *E-field* optimized a-Si:H p–i–n detector. (b) Simulated internal field profile across the i-layer of the IPD for the non-illuminated state (dark), red wavelength (red), blue wavelength (blue), and dichromatic (pink) illumination. Solid lines represent a negative *E-field;* dashed lines represent a positive *E-field*. Here, x_{cz} represents the collection zone length that equals the i-layer thickness for the dark state, 636 nm, and dichromatic illumination. 444 nm illumination leads to a field reversal at $x_{E=0}$ and thereby a reduced collection length x_{czblue}. This design enables an exploitable nonlinear photoresponse.

length to x_{czblue} = 1213 nm. The collection zone concept is essential to further explain and exploit intrinsic envelope mixing of two modulated light sources in the a-Si:H IPD.

Envelope mixing

In this section, electro-optical device simulations are presented and discussed to systematically investigate the origin of intrinsic envelope mixing at irradiance levels below mW/cm^2 considering the previously introduced collection zone (x_{cz}) concept.

In simulation, two monochromatic light sources with the wavelengths λ_1 = 444 nm (ϕ_{1peak} = 14.8 mW/cm^2) and λ_2 = 636 nm (ϕ_{2peak} = 42.4 mW/cm^2) have been modulated with a rectangular stimuli and frequencies of f_1 = 11 kHz and f_2 = 9 kHz, respectively. Light modulations have been modeled as a consecutive sequence of quasi-static DC simulations. In this scenario, the modulation frequencies f_1 and f_2 have been chosen to be far below the cut-off frequency of $f_c \approx 2.24$ MHz of the detector to ensure the reliability of the simulation method and remain the quasi-static limit in both the simulations and the measurements, thus ensuring comparability. Further details on the cut-off frequency determination are given in the section titled Methods. Considering the predefined collection zone x_{cz} allows for quantifying the maximum number of electrons $n_{cz}(t)$ that can potentially contribute to the photocurrent by integrating the amount of photogenerated electrons along the respective collection zone at a specific time t. The number of collectable electrons has been calculated taking into account the generation rate $G(x, t)$ of photo-induced charge carriers,

$$n_{cz}(t) = \int_{x_i - x_{cz}}^{x_i} G(x,t)\,dx. \tag{1}$$

In a-Si:H p–i–n photodiodes, the major photocurrent contribution can be associated with n_{cz} by neglecting hole contributions since electron mobilities exceed that of holes by orders of magnitude.[34] Figure 2(a) shows the simulation results for collectable electrons in the time domain $n_{cz}(t)$ at dichromatic illumination of $\lambda_1(f_1)$ (blue line) and $\lambda_2(f_2)$ (red line). Here, the blue and the red curve indicate the on/off pulse switching sequence for each specific light source. Due to the reduced collection zone length, the number of electrons that might contribute to a photocurrent almost vanishes for monochromatic λ_1 = 444 nm illumination. However, in the case of 636 nm and dichromatic illumination, $n_{cz}(t)$ equals the number of photogenerated electrons across the whole intrinsic absorber layer since no electric field barriers avoid electrons to drift toward the electrical contacts. The black dashed line in Fig. 2(a) shows $n_{cz}(t)$ for the case that the collection zone length equals the total absorber thickness neglecting the previously discussed *E-field* distortions. A direct

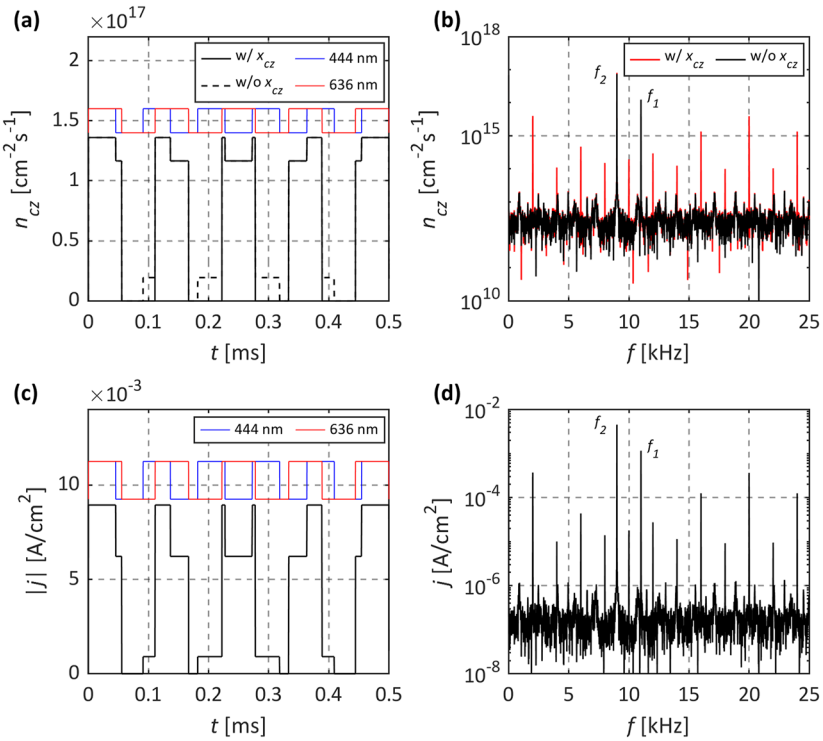

FIG. 2. Simulated number of collectable electrons n_{cz} (a) in the time and (b) in the frequency domain with and without consideration of the collection zone x_{cz} concept. Here, the blue and red lines indicate the on/off pulse sequence for the 444 nm (f_1 = 11 kHz) and 636 nm (f_2 = 9 kHz) illumination, respectively. Simulated overall detector current (c) in the time and (d) in the frequency domain. Time domain analysis reveals a significantly reduced number of collectable electrons and thereby massive current quenching at specific time positions due to reduced collection zones. Collection zone quenching results in additional mixing frequency components in the frequency domain, as shown in (d).

comparison of the simulation results for the case that I. *E-field* distortions are neglected and II. *E-field* distortions are considered [cf. Fig. 2(a)] reveals for I. the ideal superposition and for II. a nonlinearity in the number of collectable electrons $n_{cz}(t)$. The nonlinearity is indicated by additional photo-induced charge carriers of the λ_1 = 444 nm illumination. This result indicates a huge influence of deep trap-assisted *E-field* screening on the photodetectors response in the time domain. The photoresponse of sensors in the frequency domain visualized by a fast Fourier transform (FFT) of $n_{cz}(t)$ is shown in Fig. 2(b). By neglecting *E-field* distortions and local collection zone quenching/collapse, the FFT behaves almost linearly, resulting in a superposition of the two modulation signals [cf. Fig. 2(b), black solid line]. Taking the collapses of x_{cz} into account [cf. Fig. 2(b), red solid line], additional signal components in the frequency domain arise at the frequency positions $f = n \times f_1 + m \times f_2$ with $n, m \in \mathrm{Z}\backslash\{0\}$, for example, at f = 2, 4, 6 kHz, etc. Since the amount of collectable photogenerated electrons $n_{cz}(t)$ mainly determines the device current density $j(t)$,[34] this value has to have a direct impact on the sensor signal at exactly the same time positions due to the collection zone collapse, as verified in Fig. 2(c). Along the lines of previously shown n_{cz} distortions, the current features in the time domain consecutively exhibit additional mixing frequency components in the frequency domain $j(f)$ that are exactly located at $f = n \times f_1 + m \times f_2$ with $n, m \in \mathrm{Z}\backslash\{0\}$ [cf. Fig. 2(d)].

Further electro-optical simulations have been conducted to study the influence of defect density distributions within the intrinsic layer on the envelope mixing. The simulation results of the current amplitude at f_{mix} = 2 kHz are given in Table I and reveal that the envelope intensity mixing completely vanishes once the amount of deep dangling bond states is reduced significantly by ten orders of magnitude. While mixing frequency components are preserved by reducing the amount of extended tail states ten orders of magnitude and keeping the dangling bond state densities constant, sum and differential frequencies vanish once dangling bonds are reduced ten orders of magnitude in the defect model. Initial defect density values are consistent with the literature and match fundamental device characterization (cf. the supplementary material for j–V characteristics and responsivity). This result indicates that deep dangling bond states are essential to enable envelope intensity mixing in this specific device structure, material, and illumination scenario. Since the utilized fabrication technique of amorphous silicon IPDs allows to tailor material properties, including defect distributions precisely and reliably, the mixing process can be tuned toward specific applications. Furthermore, the simulations confirm the proposed hypothesis of defect-induced *E-field* screening to be the origin of envelope mixing in a-Si:H IPD. The simulation results further serve as a base for envelope mixing experiments, which are presented in the section titled Experimental results.

TABLE I. Simulated current amplitudes on the mixing frequency $f_{mix} = f_1 - f_2$ = 2 kHz for different defect distributions within the intrinsic absorber layer. More detailed information on the simulation analysis is given in the supplementary material.

	$j(f_{mix}) = j(2\ \mathrm{kHz})$ [A/cm^2]
Default defect distribution	3.7×10^{-4}
Tail state reduction	3.4×10^{-4}
Dangling bond reduction	2.2×10^{-5}
Dangling bond and tail state reduction	2.5×10^{-7}

EXPERIMENTAL RESULTS

In this section, experimental results on envelope intensity mixing in the IPD are presented. First, measurements are conducted in the kHz range to verify the simulation result within the quasi-static limit metrologically and provide a further understanding of the envelope mixing. Results in the MHz range show a proof-of-principle with settings fulfilling requirements of potential applications, e.g. optical ranging or 3D imaging, in terms of modulation frequency and irradiances of each wavelength. A schematic of the utilized setup is given in Fig. 3(c). Experimental and electro-optical simulation parameters exactly match (λ_1 = 444 nm and λ_2 = 636 nm; modulation frequencies f_1 = 11 kHz and f_2 = 9 kHz). The irradiance levels in this experiment are ϕ_1 = 14.8 mW/cm^2 and ϕ_2 = 42.4 mW/cm^2, respectively. The bias voltage of the detector has been fixed to 0 V to exclude external voltage induced influences on the build-in field. Details on the measurement procedures are given in the section titled Methods. Further details on the fabrication of the device are given in the supplementary material. Figure 3(a) shows the detector response in the time domain and the corresponding FFT signal in the frequency domain. In the time domain [cf. Fig. 3(a)], the sum of the photocurrent densities for monochromatic illumination (blue and red lines showing the modulation stimuli) significantly differs from and drops below the detector response for dichromatic illumination. This measurement result agrees with the previously derived theory presented in the section titled Electro-optical simulation. The sensor output is quenched for monochromatic λ_1 = 444 nm illumination resulting in additional signal components in the frequency domain [cf. Fig. 3(b)]. The features are located at the frequency positions $f = n \times f_1 + m \times f_2$ with $n, m \in \mathrm{Z}\backslash\{0\}$, which is in agreement with the simulation results. The delay times of the sensor visible in the photocurrent transient signals in the time domain at the positive edges of the red illumination can be attributed to filling of trap states in amorphous silicon[35] and are thus a result of the detector itself. Such time delays are not visible in reference measurements utilizing crystalline photodetectors. Since these latencies in the response time only appear at the modulation frequency, they just influence multiples of f_{mod} in the frequency domain without interacting at the intrinsic envelope mixed signals.

The signal-to-noise ratio (SNR) of the differential frequency, here located at $f_1 - f_2$ = 2 kHz, is ~40 dB, indicating I. the high-efficiency and sensitivity of the intrinsic photomixing detector and II. that irradiance levels can further be reduced in future experiments. As expected, conventional crystalline photodetectors (e.g., Hamamatsu S1337–66BK) did not show internal frequency mixing at these irradiance levels. Significantly higher irradiances would be required to enable envelope intensity mixing[17,36–38] due to the inversion symmetrical crystallographic material composition.

Most of today's optoelectronic systems and applications operate in real-time and require device operation frequencies exceeding kHz. To show the applicability of the nonlinear mixing process at higher modulation frequencies, further measurements at modulation frequencies exceeding MHz but below the device cut-off frequency have been conducted. In this experiment, the light sources limit achievable modulation bandwidth rather than the mixing

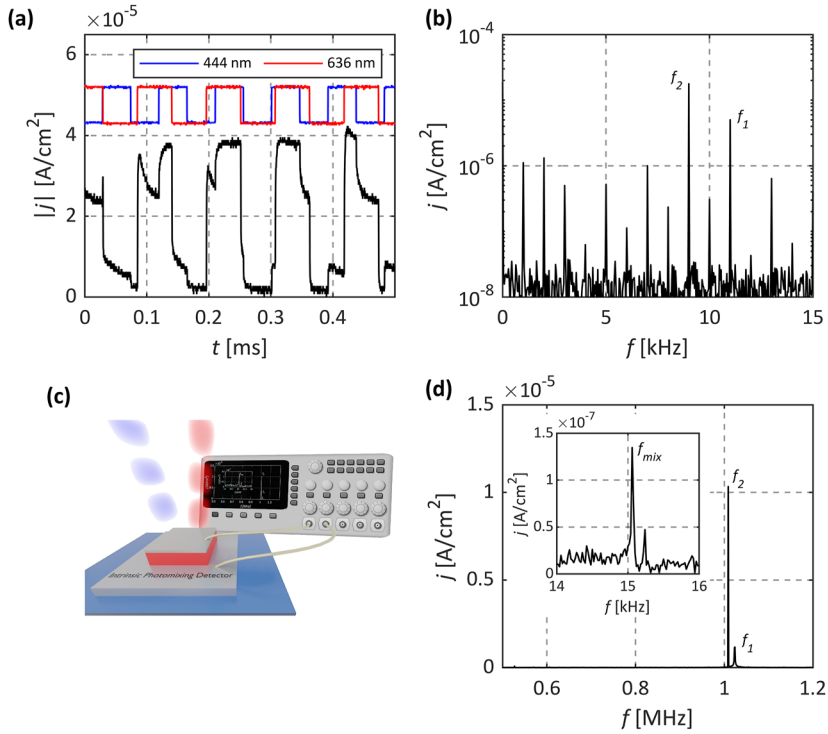

FIG. 3. Current density of the a-Si:H intrinsic photomixing detector (a) in the time and (b) the frequency domain. The blue and the red lines indicate the on/off pulse sequence for the 444 and 636 nm illumination. As predicted in the simulation section, the frequency domain FFT signal exhibits significant features at the frequency positions $f = n \times f_1 + m \times f_2$ with $n, m \in Z\backslash\{0\}$. Schematic of the measurement setup (c) and current density of the detector in the MHz regime (d). The FFT reveals the expected signal components located at the modulation frequencies f_1 (444 nm) and f_2 (636 nm). The inset shows the mixing frequency at $f_{mix} \approx$ 15 kHz generated by using a detector.

device itself. The incident light guided on the detector has been modulated using sine waveforms with frequencies of f_1 = 1.024 MHz and f_2 = 1.008 94 MHz. The irradiance levels of ϕ_1 = 4.36 mW/cm^2 and ϕ_2 = 1.03 mW/cm^2 are orders of magnitude below those required to achieve envelope mixing in high-speed graphene-based photodetectors, where irradiances of at least 300 mW/cm^2 have been reported to be mandatory[20] for mixing at frequencies beyond 60 GHz for that optimized device concept. Figure 3(d) shows the modulation amplitudes visualized in a FFT using a conventional digital oscilloscope. The inset shows the mixing frequency peak located at $f_{mix} = f_1 - f_2 \approx$ 15 kHz with a SNR of ~17 dB that is generated by the IPD itself. This result confirms that the envelope intensity mixing process in a-Si:H photodetectors is not just applicable for modulation frequencies in the kHz range but also holds true at higher f near the cut-off frequency of the device that can further be optimized. Table II summarizes the figures of merit achieved by the a-Si:H intrinsic photomixing detector presented in this work.

In the supplementary material, we further propose and demonstrate one potential application for such intrinsic photomixing devices out of amorphous silicon: optical logic AND gates. As applications advance, we believe that such logic gates might play a significant role in future high performance integrated optical communication systems, optical computing, and artificial intelligence (AI). Compared to traditional integrated electronic logic gates that typically require multiple transistors, the IPD pendant just requires one single a-Si:H device that can be fabricated at temperatures <200 °C and enables fill-factors close to 100%.[24,25] Other application examples comprise ToF 3D imaging to enable real-time 3D machine vision and machine learning,[39] innovative virtual reality and infotainment applications,[40] or robot-assisted surgery.[41] In the application as a time-of-flight 3D-imager, one wavelength would be emitted on a scene with the second wavelength acting as an internal reference signal. Measuring the phase delay on the mixing frequency allows to detect a phase delay on the detected scene-illumination signal due to the mixing process. Compared to other indirect ToF-systems, the IPD would act as a mixing device to dramatically reduce the evaluation effort of distinguishing the phase delay of the reflected scene illumination due to the lower measurement frequency. The proposed technique can enable a significant increase in pixel density at a low degree of complexity in the post-processing and potentially higher sensitivities enabled by photogating.[32] Additionally, one would result in a technology process suitable for backend CMOS integration. Thereby, it may reduce the complexity and integration effort of the sensor drastically compared to systems such as the established PMD technique. The required irradiance for envelope mixing on the longer wavelength in this proof-of-principle is just a factor of ~9 above that of a commercially available PMD flexx2 system

TABLE II. Figures of merit of the intrinsic photomixing detector operated at 0 V bias voltage.

	Wavelength [nm]	Irradiance [mW/cm^2]	Modulation frequency [Hz]	SNR @ $f_1 - f_2$ [dB]
Proof of concept	$\lambda_1 = 444$ $\lambda_2 = 636$	$\phi_1 = 14.8$ $\phi_2 = 42.43$	$f_1 = 11 \times 10^3$ $f_2 = 9 \times 10^3$	~40
MHz bandwidth	$\lambda_1 = 444$ $\lambda_2 = 636$	$\phi_1 = 4.36$ $\phi_2 = 1.03$	$f_1 = 1.024 \times 10^6$ $f_2 = 1.008\,94 \times 10^6$	~17

(116 μW/cm[42] vs 1.03 mW/cm^2), whereas significant performance enhancements of the IPD-technique are to be expected.

CONCLUSION

In this paper, intrinsic envelope intensity mixing in amorphous silicon p–i–n photodiodes, called intrinsic photomixing detectors, in the visible range has been reported. Electro-optical simulations verify that defect-induced field screening enables that mixing process. It could further be verified that deep dangling bond defect states enable mixing in this device structure and material rather than localized tail-states. Experimentally, envelope mixing has been demonstrated utilizing 444 and 636 nm illumination with irradiances below 4.5 mW/cm^2 at modulation frequencies exceeding MHz. The presented mixing is applicable in wide spreading fields, e.g., optical logic gates, time-of-flight 3D imaging, or signal generation and processing. The thin-film IPD can be fabricated at temperatures below 200 °C and can easily be integrated on top of silicon electronics with high fill factors.

METHODS

A-Si:H thin-films have been deposited by plasma-enhanced chemical vapor deposition (PECVD) at temperatures below 200 °C in a hot-wall MVS multi-chamber deposition system on pre-cleaned glass substrates. Transparent and conductive indium tin oxide (ITO) anode and cathode electrodes have been sputtered in a radio frequency hot-wall sputtering reactor at 13.56 MHz below 50 °C. The devices have been structured using standard UV-lithography to 1.6 × 1.8 mm^2, mounted in dual-inline chip carriers, and contacted via wedge bonding using a semi-automatic TPT HB16 wire bonder. Further fabrication details are given in the supplementary material and in Ref. 43. Thin-film growth rates of a-Si:H and ITO have been determined by cross-sectional back-scatter scanning electron microscopy (SEM) imaging using a FEI Quanta 250 environmental scanning electron microscope. Overall thicknesses of a-Si:H IPD have thoroughly been validated by using a Bruker Dektak XT profilometer.

Electro-optical simulations have been conducted using the simulation software AFORS-HET[26] taking into account an appropriate device model. This model has been used to subsequently develop, fabricate, and characterize the field optimized a-Si:H intrinsic photomixing detector. Low-frequency transient simulations have been performed by a set of consecutive steady-state simulations in the time domain. An overall time of 100 ms has been discretized with a resolution of 990 001 time stamps. Rectangular modulation signals serve as input parameters for the illumination sources.

Time and frequency envelope intensity mixing measurements utilize 444 nm Toptica iBEAM-SMART-PT-445CZ_20067 and 636 nm Toptica iBEAM-SMART-636-S-KL-11049 light sources. The lasers have been modulated using conventional function generators (Tektronix AFG2021 and Rhode&Schwarz HMF2550). Transient and FFT signal acquisition has been realized with a Tektronix TDS 2024C digital oscilloscope prior to an I–V conversion utilizing a Femto DHPCA100 amplifier module at a gain of 10^6. The experimental setup comprises a dichroic cube, a lens, and an optic diffuser to ensure a homogeneous illumination irradiance on the sensor. The bias voltage of the device has been fixed to 0 V to eliminate any influence on the internal electric field and thereby the defect-induced field screening.

The cut-off frequency of the device has experimentally been determined by measuring the series capacitance (122 pF) and resistance (582 Ω) using a Hewlett Packard LCR-meter.

SUPPLEMENTARY MATERIAL

The supplementary material provides in depth information on the fabrication process and basic characterization of the used a-Si:H IPD as well as electro-optical simulations including basic characterization and defect analysis of the envelope mixing process. Further, it gives LTSpice simulations of a logic Gate as one application example.

ACKNOWLEDGMENTS

The authors gratefully thank the European Regional Development Fund (Grant No. EFRE0200545) for funding this research project. Credits are given to the Micro- and Nanoanalytics Facility (MNaF) of the University of Siegen for sample analyses. Open Access funding was made possible by the University Library Siegen.

AUTHOR DECLARATIONS

Conflict of Interest

The authors have no conflicts to disclose.

Author Contributions

M.M., A.B., and R.B. contributed equally to this work and should be considered co-first authors.

Maurice Müller: Data curation (equal); Formal analysis (equal); Investigation (equal); Methodology (equal); Validation (equal);

Visualization (equal); Writing – original draft (equal). **Andreas Bablich**: Conceptualization (equal); Investigation (equal); Methodology (equal); Resources (equal); Validation (equal); Writing – original draft (equal). **Rainer Bornemann**: Conceptualization (equal); Resources (equal); Software (equal); Writing – review & editing (equal). **Nils Marrenbach**: Investigation (supporting); Writing – review & editing (equal). **Paul Kienitz**: Resources (equal); Validation (equal); Writing – review & editing (equal). **Peter Haring Bolívar**: Funding acquisition (lead); Project administration (lead); Supervision (lead); Writing – review & editing (equal).

DATA AVAILABILITY

The data that support the findings of this study are available from the corresponding author upon reasonable request.

REFERENCES

[1] D. E. Carlson and C. R. Wronski, "Amorphous silicon solar cell," Appl. Phys. Lett. **28**, 671 (1976).
[2] P. G. le Comber, W. E. Spear, and A. Ghaith, "Amorphous-silicon field-effect device and possible application," Electron. Lett. **15**, 179 (1979).
[3] D. H. Auston, P. Lavallard, N. Sol, and D. Kaplan, "An amorphous silicon photodetector for picosecond pulses," Appl. Phys. Lett. **36**, 66 (1980).
[4] Q. Zhu, S. Coors, B. Schneider, P. Rieve, and M. Bohm, "Bias sensitive a-Si(C): H multispectral detectors," IEEE Trans. Electron Devices **45**, 1393 (1998).
[5] G. D. Cody, T. Tiedje, B. Abeles, B. Brooks, and Y. Goldstein, "Disorder and the optical-absorption edge of hydrogenated amorphous silicon," Phys. Rev. Lett. **47**, 1480 (1981).
[6] J. Chevallier, H. Wieder, A. Onton, and C. R. Guarnieri, "Optical properties of amorphous Si_xGe_{1-x}(H) alloys prepared by R.F. glow discharge," Solid State Commun. **24**, 867–869 (1977).
[7] J. Bullot, M. Gauthier, M. Schmidt, Y. Catherine, and A. Zamouche, "Electronic and optical properties of glow-discharge amorphous silicon-carbon alloys," Philos. Mag. B **49**, 489 (1984).
[8] P. G. Le Comber and W. E. Spear, "Electronic transport in amorphous silicon films," Phys. Rev. Lett. **25**, 509 (1970).
[9] R. C. Chittick, J. H. Alexander, and H. F. Sterling, "The preparation and properties of amorphous silicon," J. Electrochem. Soc. **116**, 77 (1969).
[10] K.-Y. Wang and A. C. Foster, "Ultralow power continuous-wave frequency conversion in hydrogenated amorphous silicon waveguides," Opt. Lett. **37**, 1331 (2012).
[11] K. Li and A. C. Foster, "1.25-Gb/s all-optical NAND/AND logic gates in a hydrogenated amorphous silicon waveguide," in *Conference on Lasers and Electro-Optics (2017), Paper SM1M.3* (Optical Society of America, 2017), p. SM1M.3.
[12] A. K. M. Lam, M. Fairburn, and N. A. F. Jaeger, "Wide-band electrooptic intensity modulator frequency response measurement using an optical heterodyne down-conversion technique," IEEE Trans. Microwave Theory Tech. **54**, 240 (2006).
[13] Z. Tang, Y. Li, J. Yao, and S. Pan, "Photonics-based microwave frequency mixing: Methodology and applications," Laser Photonics Rev. **14**, 1800350 (2020).
[14] F. Zhang, G. Sun, Y. Zhou, B. Gao, and S. Pan, "Towards high-resolution imaging with photonics-based time division multiplexing MIMO radar," IEEE J. Sel. Top. Quantum Electron. **28**, 1 (2022).
[15] M. Kumar and V. K. Tripathi, "Terahertz generation by nonlinear mixing of laser pulses in a clustered gas," Phys. Plasmas **18**, 053105 (2011).
[16] M. DiDomenico, R. H. Pantell, O. Svelto, and J. N. Weaver, "Optical frequency mixing in bulk semiconductors," Appl. Phys. Lett. **1**, 77 (1962).
[17] O. Svelto, P. D. Coleman, M. DiDomenico, and R. H. Pantell, "Photoconductive mixing in CdSe single crystals," J. Appl. Phys. **34**, 3182 (1963).
[18] R. P. Riesz, "High speed semiconductor photodiodes," Rev. Sci. Instrum. **33**, 994 (1962).
[19] C. Cheng, B. Huang, X. Mao, Z. Zhang, Z. Zhang, Z. Geng, P. Xue, and H. Chen, "Frequency conversion with nonlinear graphene photodetectors," Nanoscale **9**, 4082 (2017).
[20] A. Montanaro, W. Wei, D. De Fazio, U. Sassi, G. Soavi, P. Aversa, A. C. Ferrari, H. Happy, P. Legagneux, and E. Pallecchi, "Optoelectronic mixing with high-frequency graphene transistors," Nat. Commun. **12**, 2728 (2021).
[21] L. Hamidouche, A. Montanaro, M. Rosticher, E. Grimaldi, B. Poupet, T. Taniguchi, K. Watanabe, B. Plaçais, E. Baudin, and P. Legagneux, "Optoelectronic mixing in high-mobility graphene," ACS Photonics **8**, 369 (2021).
[22] I. C. F. S. Condotta, T. M. Brown-Brandl, S. K. Pitla, J. P. Stinn, and K. O. Silva-Miranda, "Evaluation of low-cost depth cameras for agricultural applications," Comput. Electron. Agric. **173**, 105394 (2020).
[23] R. Lange, S. Böhmer, and B. Buxbaum, CMOS-based optical time-of-flight 3D imaging and ranging, *High Performance Silicon Imaging* (Elsevier, 2020), pp. 319–375.
[24] T. Lule, S. Benthien, H. Keller, F. Mutze, P. Rieve, K. Seibel, M. Sommer, and M. Bohm, "Sensitivity of CMOS based imagers and scaling perspectives," IEEE Trans. Electron Devices **47**, 2110 (2000).
[25] F. Lemmi, J. T. Rahn, and R. A. Street, "Lateral conduction in structured amorphous silicon P^+–i–N^+ photodiodes," J. Non-Cryst. Solids **266–269**, 1203 (2000).
[26] R. Varache, C. Leendertz, M. E. Gueunier-Farret, J. Haschke, D. Muñoz, and L. Korte, "Investigation of selective junctions using a newly developed tunnel current model for solar cell applications," Sol. Energy Mater. Sol. Cells **141**, 14 (2015).
[27] M. Müller, A. Bablich, P. Kienitz, R. Bornemann, C. O. Ogolla, B. Butz, and P. Haring Bolívar, "High-sensitivity focus-induced photoresponse in amorphous silicon photodiodes for enhanced three-dimensional imaging sensors," Phys. Rev. Appl. **17**, 034075 (2022).
[28] R. S. Crandall, "Modeling of thin-film solar cells: Nonuniform field," J. Appl. Phys. **55**, 4418 (1984).
[29] M. Hack and M. Shur, "Physics of amorphous silicon alloy *p–i–n* solar cells," J. Appl. Phys. **58**, 997 (1985).
[30] K. Misiakos and F. A. Lindholm, "Analytical and numerical modeling of amorphous silicon *p–i–n* solar cells," J. Appl. Phys. **64**, 383 (1988).
[31] J.-H. Zollondz, S. Reynolds, C. Main, V. Smirnov, and I. Zrinscak, "The influence of defects on response speed of high gain two-beam photogating in a-Si:H PIN structures," J. Non-Cryst. Solids **299–302**, 594 (2002).
[32] C. Main, J.-H. Zollondz, S. Reynolds, W. Gao, R. Brüggemann, and M. J. Rose, "Investigation of collection efficiencies much larger than unity in a-Si:H p–i–n structures," J. Appl. Phys. **85**, 296 (1999).
[33] S. Reynolds, C. Main, V. Smirnov, and A. Meftah, "Intensity dependence of quantum efficiency and photo-gating effects in thin film silicon solar cells," Phys. Status Solidi C **7**, 505 (2010).
[34] R. A. Street, *Hydrogenerated Amorphous Silicon* (Press Syndicate of the University of Cambridge, Cambridge, 1991).
[35] C. Ulrichs, T. Eickhoff, and H. Wagner, "Transient response of the photocurrent in a-Si:H layers and solar cells," J. Non-Cryst. Solids **164–166**, 705 (1993).
[36] M. M. Fejer, "Nonlinear optical frequency conversion," Phys. Today **47**(5), 25 (1994).
[37] N. Bloembergen, R. K. Chang, S. S. Jha, and C. H. Lee, "Optical second-harmonic generation in reflection from media with inversion symmetry," Phys. Rev. **174**, 813 (1968).
[38] N. Bloembergen and P. S. Pershan, "Light waves at the boundary of nonlinear media," Phys. Rev. **128**, 606 (1962).
[39] S. Zhang, *Handbook of 3D Machine Vision: Optical Metrology and Imaging* (CRC Press, 2013).
[40] A. Kolb, E. Barth, R. Koch, and R. Larsen, "Time-of-flight cameras in computer graphics," Comput. Graph. Forum **29**, 141 (2010).
[41] J. K. Udupa and G. T. Herman, *3D Imaging in Medicine*, 2nd ed. (CRC Press, 1999).
[42] pmdtechnologies, Pmd, Flexx2 3D Camera Development Kit, https://3d.pmdtec.com/en/3d-cameras/flexx2/.
[43] A. Bablich, C. Merfort, H. Schäfer-Eberwein, P. Haring-Bolivar, and M. Boehm, "2-in-1 red-/green-/blue sensitive a-SiC:H/a-Si:H/a-SiGeC:H thin film photo detector with an integrated optical filter," Thin Solid Films **552**, 212 (2014).